

Fermi-surface topological phase transition and horizontal order-parameter nodes in CaFe_2As_2 under pressure

R. S. Gonnelli,^{1*} D. Daghero,¹ M. Tortello,¹ G. A. Ummarino,¹ Z. Bukowski,² J. Karpinski,³ P. G. Reuvekamp,⁴ R. K. Kremer,⁴ G. Profeta⁵, K. Suzuki⁶ and K. Kuroki⁷

¹*Dipartimento di Scienza Applicata e Tecnologia, Politecnico di Torino, Torino, Italy*

²*Włodzimierz Trzebiatowski Institute of Low Temperature and Structure Research, Polish Academy of Sciences, 50-950 Wrocław, Poland*

³*Laboratoire de Physique de la matière condensée, Ecole Polytechnique Fédérale de Lausanne, CH-1015 Lausanne, Switzerland*

⁴*Max Planck Institute for Solid State Research, Stuttgart, Germany*

⁵*Dipartimento di Scienze Fisiche e Chimiche, Università dell'Aquila, L'Aquila, Italy*

⁶*Department of Engineering Science, The University of Electro-Communications, Chofu, Tokyo 182-8585, Japan*

⁷*Department of Physics, Osaka University, 1-1 Machikaneyama, Toyonaka, Osaka 560-0043, Japan*

* To whom correspondence should be addressed. E-mail: renato.gonnelli@polito.it

Abstract

Iron-based superconductors (IBS) display a surprising variety of properties that seems to arise from the strong sensitivity of these systems to tiny details of the lattice structure. In this respect, systems that become superconducting under pressure, like CaFe_2As_2 , are of particular interest. Here we report on the first directional point-contact Andreev-reflection spectroscopy (PCARS) measurements on CaFe_2As_2 crystals under quasi-hydrostatic pressure, and on the interpretation of the results using a 3D model for Andreev reflection combined with *ab-initio* calculations of the Fermi surface (within the Density Functional Theory) and of the order-parameter (OP) symmetry (within a Random Phase Approximation approach in a ten-orbital model). The almost perfect agreement between PCARS results at different pressures and theoretical predictions highlights the intimate connection between the changes in the lattice structure, a 2D-3D topological transition in the hole-like Fermi surface sheet, the emergence on the same sheet of an OP with a horizontal node line and a considerable increase in the electron-boson coupling.

Since 2008 different families of IBS have been discovered [1][2] and numerous compounds within each family have been synthesized. All their phase diagrams look qualitatively similar [3] and indicate the proximity of superconductivity to a magnetically ordered phase. The Fermi surface (FS) of the parent compounds generally features hole-like and electron-like sheets connected by a $(\pi-\pi)$ wavevector (associated to the AFM order). These two facts led to the hypothesis of a superconducting pairing mediated by spin fluctuations, which in turn would lead to order parameters (OPs) of opposite sign on the hole-like and electron-like FS sheets (the so-called s_{\pm} symmetry) [4].

Despite the general consensus around this picture, representative counterexamples have been recently discovered, i.e. superconducting compounds which possess only electron-like or hole-like FS, such as FeSe monolayers on SrTiO₃ [5], KFe₂As₂ [6], K_{0.8}Fe_{1.7}Se₂ [7]. The disappearance of a FS sheet (Lifshitz transition) was already recognized in, at least, another compound, namely CaFe₂As₂ under pressure. The phase diagram of CaFe₂As₂ presents four temperature-driven phase transitions: At ambient pressure, the tetragonal–orthorhombic (T-OR) structural transition accompanied by the paramagnetic–antiferromagnetic (PM-AFM) transition; and, under pressure, the tetragonal–collapsed tetragonal (T-cT) structural transition, and the superconducting transition [8][9]. In the cT phase, stable at low temperature under hydrostatic pressure, the out-of-plane *c* lattice constant is shorter by 10% than in the T phase; ARPES shows that the hole-like FS is not present at Γ [10] (and consistent results are given by transport, Hall effect and Seebeck measurements [11]) while inelastic neutron scattering experiments indicate the absence of spin fluctuations [12][13]. Indeed, this phase is not superconducting [14]. Hence, the superconductivity observed in CaFe₂As₂ under pressure [8][9] was supposed to emerge from some paramagnetic “non-collapsed tetragonal” phase [15] close to a magnetic instability. Such a tetragonal phase was indeed observed experimentally and stabilized by non-hydrostatic pressure conditions [16]. The

tight relation between crystal structure and superconducting properties is confirmed by aliovalent-doped CaFe_2As_2 (with rare-earth atoms substituting Ca) which shows both a superconducting phase with high critical temperature (T_c) up to 47 K [17] and a structural phase transition to the non-magnetic cT phase with closed hole-like FS pockets [15].

Pressure can thus drive CaFe_2As_2 across a structural and electronic transition that makes it bridge the gap between “usual” multiband IBS and “anomalous” single-band ones, and is associated with the emergence of a high- T_c superconducting phase – though the question about which lattice structure supports this phase is still open. To shed light on the role of the closeness of the cT phase to the superconducting phase, on the importance of the Lifshitz transition in the appearance of superconductivity in IBS, and on the effects of this transition on the symmetry of the OP, we designed a dedicated experimental study of the superconducting OP of CaFe_2As_2 as a function of the cell deformation (in the region of the T-cT transition). To avoid the possible complications related to chemical substitutions, we induced this deformation in CaFe_2As_2 single crystals by means of anisotropic pressure. To determine the amplitude and symmetry of the OP, we used a energy-resolved, directional spectroscopic technique (point-contact Andreev-reflection spectroscopy, PCARS) and interpreted the experimental results with the aid of first-principles and Random Phase Approximation (RPA) calculations. In correspondence to the structural transition between the OR phase and the cT phase, we observe a topological 2D-3D transition in the hole-like FS. This transition is accompanied by the emergence of a horizontal line node in the relevant OP, by an increase in T_c and an even greater increase in the OP amplitudes that suggests a considerable enhancement of the electron-boson coupling.

Point-contact Andreev-reflection spectroscopy under non-hydrostatic pressure

In a PCARS experiment the differential conductance dI/dV of a nanoscopic contact between a normal metal (N) and a superconductor (S) is measured as a function of V (I and V being the probe

current through the contact and the voltage at the contact's ends, respectively). Under suitable conditions (in particular, if the contact diameter is smaller than the electron mean free path [18] and the potential barrier at the interface is small) the differential conductance contains quantitative information about the amplitude and the symmetry of the superconducting gap thanks to the quantum phenomenon called Andreev reflection (see Supplementary Information for details). The standard way for obtaining the point contact is the so-called needle-anvil technique, in which a sharp normal-metal tip is pressed against the surface of the superconductor [18]. This technique is not applicable for operations in high-pressure cells at low temperatures. We thus adopted an alternative technique ("soft" point-contact technique) wherein the contact tip is substituted by a tiny silver paste contact whose resistance can be tuned via short current pulses [19]. This method can be easily adapted to work in a pressure cell, as in the present case.

The PCARS measurements were performed on Sn-flux grown CaFe_2As_2 single crystals at temperatures down to 1.2 K and at pressures between 0.4 and 0.85 GPa utilizing a CuBe clamp cell whose schematic drawing is shown in Fig. 1a. The pressure-transmitting medium is silicone oil, hence the pressure is hydrostatic as long as the oil remains liquid. When the oil freezes, instead, the pressure becomes quasi-hydrostatic, acquiring a uniaxial component that is essential for the stabilization of the low-temperature tetragonal phase and the onset of superconductivity in CaFe_2As_2 [14][16]. Fig. 1b shows a scheme of the sample holder, with the crystal mounted on one side and the Ag-paste contact on the crystal surface. Fig. 1c represents a detail of the crystal with the point contact and the indication of the current and voltage leads used for PCARS experiments. Further details on the experimental setup can be found in the section Methods.

Figures 1d and 1e display raw PCARS spectra (dI/dV vs. V) measured at different temperatures and at pressures P of 0.40 GPa and 0.61 GPa, respectively. In these cases the contacts were placed on the side edges of a CaFe_2As_2 crystal, so that the probe current I was preferentially injected parallel to the ab planes. The slightly concave shape of the high-voltage tails and their superposition

indicate that the point contacts fulfill the requirements to be spectroscopic: electrons are not diffused while crossing the contact region so that there is no Joule heating. The same considerations apply to the spectra shown in Fig. 1f, which were measured with the current injected along the c axis at $P = 0.53$ GPa. The temperature at which the structures in the dI/dV spectra disappear and the *whole* conductance curve becomes temperature independent in the following will be called “Andreev critical temperature” T_c^A . The absence of Joule heating effects in the contact is also assured by the good agreement of T_c^A and the bulk T_c determined from resistivity measurements at the same pressure [8].

Despite the different current injection direction, the low-temperature spectra in Figures 1d, 1e and 1f are remarkably similar. They contain a zero-bias maximum and additional broad structures (shoulders) at about 3-5 mV. These can be better resolved when the curves are normalized, i.e. when the differential conductance of the N-S contact is divided by the conductance of the same contact in the normal state, $(dI/dV)_{NN}$ (in this case, we divided by the conductance curve just above T_c^A). The thus normalized conductance at the lowest temperature is shown in the insets to Figures 1d-1f. All the spectra measured on different contacts (more than 25) at different pressures and along different crystallographic directions always show the same features. In particular, the zero-bias conductance peak (ZBCP) is always present and is not suppressed by magnetic fields up to 6 T (see Fig. 1g) [20].

Taking into account the temperature and magnetic-field dependence of the spectra along the ab plane shown in Fig. 1d, 1e and 1g the only way to interpret the data is to admit that the OP presents lines of nodes (or zeros) on the Fermi surface (FS) [19][21]. However, any attempt to fit the normalized PCARS spectra by using the 2D Blonder-Tinkham–Klapwijk (BTK) model [21] with a single nodal gap fails, demonstrating that multiple gaps (at least two, of different amplitude) are necessary. If the larger gap is taken to be isotropic and the smaller one is instead assumed to have lines of nodes or zeros, the 2D BTK model can reproduce the ab -plane results very well. However

this procedure is not correct because: a) the FS of CaFe_2As_2 at these pressures is not as 2D-like as in other Fe-based compounds [22] and thus the 2D BTK model is oversimplified; b) this procedure completely fails in reproducing the ZBCPs observed in PCARS experiments with current injection along the c axis (Fig. 1f).

Fermi-surface topology and order-parameter structure

To coherently explain the PCARS results both along the ab plane and the c -axis direction the analysis requires the inclusion of the actual shape of the FS sheets and a detailed knowledge of the order-parameter structure. We recently introduced a 3D extension of the BTK model for calculating the Andreev-reflection (AR) normalized conductance by taking into account the FS topology in a simplified way [19][23]. Within this model the normalized conductance at $T=0$ for current injected along the direction \mathbf{n} – given that the effective-mass approximation holds – can be described by the following expression,

$$\langle G(E) \rangle_{I//n} = \frac{\sum_i \left\langle \sigma_{ik,n}(E) \tau_{ik,n} \frac{v_{ik,n}}{v_{ik}} \right\rangle_{FS_i}}{\sum_i \left\langle \tau_{ik,n} \frac{v_{ik,n}}{v_{ik}} \right\rangle_{FS_i}}$$

where $v_{ik,n}$ is the projection of the k -dependent Fermi velocity in the i -th band along the \mathbf{n} direction and $\langle \rangle_{FS_i}$ represents the average over the i -th FS sheet. $\tau_{ik,n}$ is the normal-state barrier transparency which depends on $v_{ik,n}$, on the Fermi velocity in the normal material (assumed constant in magnitude) and on the barrier height at the NS interface (represented by a dimensionless parameter Z_i). Finally $\sigma_{ik,n}(E)$ is the relative barrier transparency in the superconducting state expressed as a function of $\tau_{ik,n}$ and of the k -dependent OPs Δ_{ik}^+ and Δ_{ik} of the i -th band felt by the electron-like and hole-like quasiparticles, respectively [19][23]. The knowledge of the FS topology and of the k dependence of the order parameters (i.e. their

symmetry) thus allows calculating the normalized conductance at any temperature (using the standard convolution with the Fermi function).

For this reason we studied, by means of first-principles Density Functional Theory (DFT), the effects of a uniaxial pressure on the band structure and the FS of CaFe_2As_2 . Starting from the equilibrium configuration at $P=0$ we reduced the out-of-plane c lattice constant leaving the in-plane lattice constant fixed at its equilibrium value ($a= 3.925079 \text{ \AA}$). This approximation is justified by the observation that in the examined pressure range (up to 6 GPa) the a lattice constant decreases only by about 1%, whereas the c lattice constant by about 10% [24]. The equilibrium crystal structure at any value of the c/a ratio is obtained by determining the internal parameter h_{As} (the height of the As atoms above the Fe layer) that minimizes the total energy and by considering the AFM phase for the orthorhombic structure and the non-magnetic phase for the tetragonal structure [15]. In Fig. 2a, we report the total energy of the crystal and the calculated magnetic moment in both the AFM and non-magnetic phase versus the c/a ratio. The equilibrium structure at $P=0$ ($c/a = 1.4466$, magnetic moment $\sim 1.5 \mu_{\text{B}}$) corresponds to the minimum energy in the AFM OR phase. With decreasing c/a ratio the energy of the AFM phase increases and for $c/a < 1.3826$ the system exhibits a sharp first-order phase transition towards a non-magnetic phase. We associate the narrow region around this c/a value to the non-collapsed tetragonal phase where superconductivity is thought to exist [16]. With the increase of pressure, the total energy exhibits a pronounced second minimum at $c/a= 1.3570$, which is related to the existence of the so-called collapsed-tetragonal (cT) phase. Indeed, its c/a value is in excellent agreement with the value calculated under hydrostatic conditions [24]. Interestingly, at the c/a value corresponding to the onset of the phase transition the pnictogen height h_{As} and the angle of the tetrahedron formed by Fe-As-Fe bonds suddenly jump to values close to the “optimal” ones observed at the maximum T_c for most of the Fe-based compounds, as shown in the inset to Fig. 2a.

The electronic band structure of CaFe_2As_2 is displayed in Fig. 2b for three representative values of c/a corresponding to: the equilibrium structure at $P=0$ (top panel); the tetragonal structure T^* at the beginning of the phase transition (middle panel); the equilibrium cT structure (bottom panel). The corresponding FSs are shown in Fig. 2c, from top to bottom. At $P=0$ the characteristic features of the electronic band structure of the 122 compounds are seen, i.e.: three almost cylindrical hole-like FSs (one of which has larger radius on the $k_z=\pi$ plane) centered at the Γ point and two (also 2D-like) electron-like FSs centered at the X point of the BZ. By increasing the pressure along the z direction to the c/a ratio 1.3826, dramatic effects on the shape of the FSs are noticed: the two inner hole bands are completely filled at the Γ point and thus the two relevant 2D-like Fermi cylinders centered at Γ turn into two 3D Fermi pockets of approximately ellipsoidal shape centered around the Z point, one inside the other. The outer holelike FS further expands on the $k_z=\pi$ plane but strongly shrinks at $k_z=0$. The two electron-like FS sheets are still present, even though the inner one is strongly reduced. Finally in the cT phase (lower panel), characterized by the complete suppression of the Fe magnetic moment, the inner hole bands are completely filled at both the Γ and the Z points of the BZ, where they touch the Fermi level. The outer hole band exhibits full 3D character, crossing the Fermi level along the Γ - Z line.

These results demonstrate how the reduction of the c lattice constant under uniaxial pressure induces a 2D to 3D topology change of the holelike Fermi surfaces, associated to the filling of the hole bands at the Γ point and to the complete suppression of the magnetic properties. The intermediate phase T^* is on the verge of this transition but still retains a very small hole-like FS at the Γ point and a magnetic moment, and is characterized by almost-optimal values of h_{As} and of the Fe-As-Fe angle. It is thus licit to assume this phase to be close to the one in which optimal superconducting properties are observed.

Once the band structure and the shape of the FS are known, it is possible to calculate the expected symmetry and the *relative* amplitude of the order parameters on the different sheets of the FS.

The calculations were performed following the method adopted in [25] for $\text{BaFe}_2(\text{As,P})_2$ where horizontal nodes in the superconducting gap were obtained on the warped portion of the hole Fermi surface. Starting from the first-principles DFT band structure in the region of the 2D-3D phase transition (middle panel of Fig. 2b) we constructed a ten-orbital model which takes into account all five 3d orbitals (times 2 Fe atoms per unit cell) exploiting the maximally localized Wannier functions. We subsequently applied a RPA approach to this model in order to obtain the spin susceptibility. Finally, the linearized Eliashberg equations were solved using a pairing interaction proportional to the RPA spin susceptibility (plus the charge susceptibility which has minor effect). The eigenfunctions viz. the superconducting gaps are summarized in Fig. 2d at different k_z values for the two FS sheets (the quasi-3D outer hole sheet and the quasi-2D outer electron sheet) considered in our model. A horizontal cut of the FS at $k_z = \pi$ and a vertical cut at $k_x - k_y = 0$ are shown in Fig. 2e.

The gap on the electron FS is relatively isotropic (except at $k_z = \pi$), while the gap on the hole FS is smaller and strongly anisotropic in the ab plane. Moreover, the latter decreases with the decrease of k_z until it changes sign at a k_z value of about $3\pi/4$ forming a horizontal node line [26].

Determination of energy gap amplitudes from experimental data

These results can be used for the construction of the analytical models of the FS and of the OP symmetry used in our 3D BTK model. Fig. 3a displays a pictorial representation of both models. The electron FS (one half of the total one) is modeled by a one-sheeted hyperboloid of revolution (yellow surface). Its gap Δ_e is taken to be isotropic (gridded surface). For the hole FS (again one half of the total one) an oblate spheroid can be utilized (light blue surface). As a matter of fact, the small cylindrical region of the hole FS around Γ gives a very small (or null, for current injection along the c axis) contribution to the conductance, and can thus be neglected; as a consequence, a small hole in the bottom of the spheroid has to be taken into account. Following the results of Fig.

2d, the gap Δ_h (gridded surface) exhibits a strong anisotropy in the ab plane ($\Delta_h^{\max} = 3\Delta_h^{\min}$) as well as a horizontal node line at $k_z \sim 3\pi/4$. An analytical expression for this gap symmetry can be easily given in terms of the azimuth and inclination angles θ and ϕ in the k space (see Methods). All the dimensions of the model FSs have been fixed by a comparison with the FSs calculated by DFT (see middle panel of Fig. 2c).

Finally, we are able to use the 3D BTK model to fit the experimental conductance curves. The absolute amplitudes of the superconducting gaps on the electronlike and holelike bands, Δ_e and Δ_h , cannot be predicted accurately by RPA in the ten-orbital model and are thus taken as adjustable parameters, as well as the barrier height parameters Z_e and Z_h . To account for the reduction in amplitude of the conductance curves in a phenomenological way, we also included two lifetime-broadening parameters Γ_e and Γ_h [23]. The relative weight of the hole band in the total conductance is instead fixed by the FS geometry and the direction of current injection. The results of the fits are shown in Fig. 3b, c and d for ab -plane contacts at different pressures (0.40, 0.61 and 0.85 GPa, respectively) and in Fig. 3e for a c -axis contact at 0.53 GPa. In all cases the agreement between the experimental curves (open circles) and the fits (red lines) is very good. Similar results have been obtained for nine different contacts at different pressures. The 3D BTK fits give very good results also in the analysis of the temperature dependency of the conductance curves. It turns out that both Δ_e and Δ_h approximately follow the BCS temperature dependence with noticeable deviations at $T > T_c/2$ (see Supplementary Information).

Pressure dependence of the electron-boson coupling

The critical temperature of the contacts, T_c^A , and the gaps Δ_e and Δ_h determined by the 3D BTK fit of PCARS spectra are displayed in Fig. 4a as a function of the pressure. T_c^A follows remarkably well

the behaviour of the bulk critical temperature, which shows a broad maximum at pressures between ~ 0.6 and 0.75 GPa [8].

With increasing pressure both the hole and the electron gaps behave similarly: after a region with almost constant values ($0.4 - 0.55$ GPa) they grow rapidly between 0.55 and 0.6 GPa before decreasing again for $P \geq 0.8$ GPa. The rate of increase in this narrow pressure region is definitely larger than that exhibited by T_c^A , with more than a doubling of the gap values within a pressure range of only 0.1 GPa. This behaviour is reminiscent of a quantum phase transition and occurs exactly in the small pressure range where our DFT calculations detected the 2D – 3D topological phase transition. As a consequence, the ratios $2\Delta/k_B T_c$ for the hole and the electron gaps exhibit a dramatic increase in this pressure region as illustrated in Fig. 4b. At $P < 0.55$ GPa this ratio for the holes is very small ($1 - 1.5$) while for the electrons it is slightly larger than the BCS value (horizontal dashed line in Fig. 4b). Between 0.6 and 0.75 GPa, instead, the ratio for holes is above the BCS value, and that for electrons reaches values of the order of 8 . The growth of the ratio in the pressure range between 0.4 GPa and 0.6 GPa turns out to be of the order of 75% and 180% for electrons and holes, respectively.

The sharp increase in both the hole-like and electron-like OPs and in the corresponding gap ratios suggests an important increase of the electron-boson coupling strength in the same narrow pressure range where the topological 2D-3D transition of the hole-like FS occurs. The same topological transition drives the emergence of a horizontal line of nodes in the OP residing on the hole-like FS sheet, which leaves its fingerprints in the behaviour of the zero-bias Andreev-reflection conductance. It is intriguing to notice that the same phase transition with disappearance of the hole-like FS at Γ that here produces a dramatic increase of the coupling in both the bands seems to be responsible for the high- T_c phase at 47 K observed in rare-earth doped CaFe_2As_2 [17], and for the second, higher- T_c superconducting dome in $\text{LaFeAsO}_{1-x}\text{H}_x$ [34].

Here the unique combination of directional point-contact Andreev-reflection spectroscopy on a sample under pressure and state-of-the-art *ab*-initio calculations demonstrates the dominant role of a 2D-3D topological phase transition of the hole-like FS and of the horizontal-line node in the “hole” gap in the superconductivity of the Fe-based compound CaFe_2As_2 . This approach can provide a new comprehensive tool for the fundamental investigation of the effect on superconductivity of subtle changes in the Fermi-surface topology.

Methods

Growth and characterization of the crystals

The CaFe_2As_2 single crystals were grown in a Sn flux, starting from atomic ratios $\text{Ca}:\text{Fe}:\text{As}:\text{Sn}=1.1 : 2 : 2.1 : 40$. The components, contained in alumina crucibles, were placed in sealed quartz ampoules previously filled with Ar gas under a pressure of 0.3 bar. The ampoules were then slowly heated (~ 4 h) to 600°C , held at this temperature for 1 h, then further heated (~ 5 h) to 1050°C , and kept at this temperature for 5 h so that all the components dissolved in the Sn flux. Crystals were grown by slow cooling the melt at a rate of 2 K/h to 600°C , followed by furnace cooling to room temperature. The flux was finally removed by etching in diluted hydrochloric acid.

The resulting single crystals were platelike, with the *c*-axis perpendicular to the plate, and had typical sizes of $\sim 5.0 \times 4.0 \times 0.2 \text{ mm}^3$. The crystals used for PCARS measurements had a smaller size (about $2.0 \times 1.5 \times 0.1 \text{ mm}^3$). Phase purity was checked by powder x-ray diffraction (XRD). The details of the characterization can be found in Ref. [27].

Experimental setup for point-contact measurements

The point contacts were made by using the so-called “soft” technique [19], i.e. by putting a small drop of Ag paste ($\varnothing \sim 50 \mu\text{m}$) acting as normal-metal counterelectrode on the freshly cleaved surface of the crystal. A varying probe current I was then injected from the Ag spot into the superconductor and the voltage V across the contact was measured, thus determining the I - V characteristics of the contact. Note that if the contact is put on the topmost surface, the current is mainly injected along the *c* axis; if it is placed on the side surface, the current is preferentially injected along the *ab* planes. With respect to the conventional needle-anvil technique (where the point contact is created by pressing a sharp metallic tip against the sample surface) this technique has several advantages, i.e. it ensures a greater mechanical, thermal and electrical stability of the contacts, it allows the whole setup to be mounted

on a small support, and it does not require any mechanical action from external moving parts. The latter point is fundamental, since for the present measurements the whole setup has to be closed in a pressure cell with no possibility of mechanical manipulation from outside.

The sample holder was made from a small ($\sim 7 \times 3 \text{ mm}^2$) Fiberglass board, with a small 50-turn coil wrapped around a piece of high-purity Pb (99.9999%) placed on the reverse side. The sample holder was mounted in a Cu-Be pressure cell and immersed in silicon oil used as pressure medium ensuring quasi-hydrostatic pressure conditions below the freezing point of the oil. The pressure was applied at room temperature. Subsequently, the cell was cooled in a ^4He variable temperature cryostat. To determine the pressure at low temperature, we measured the temperature of the superconducting transition of Pb by an ac mutual inductance technique.

DFT and RPA *ab-initio* calculations

The *ab-initio* DFT calculations were performed within the generalized gradient approximation (GGA) for the exchange-correlation functional using the PBE approach [28]. The pseudopotential method was employed to describe the electron-ion interaction using the Vienna *ab-initio* Simulation Package, but all-electron full-potential codes (Wien2K [29], Elk [30]) were also used in order to compare the results and confirm the findings.

For the structural optimization (always done in the antiferromagnetic phase) the charge density was integrated with $8 \times 8 \times 4$ k-points in the Brillouin zone. The band structures were always calculated in the non-magnetic body-centered tetragonal phase (irrespective of their ground state).

For the construction of the ten-orbital model that takes into account all five 3d orbitals we exploited the maximally localized Wannier orbitals [31] by using the code developed by A. A. Mostofi et al. for the generation of the Wannier functions [32] starting from first-principles band structure obtained with Quantum Espresso [33]. As for the electron-electron interactions, we considered the intra-orbital $U=1.56$, the inter-orbital $U'=1.17$, Hund's coupling and the pair hopping interaction $J=J'=0.195$. In the RPA calculations used to obtain the spin susceptibility on $16 \times 16 \times 16$ k-point meshes, 512 Matsubara frequencies were used and the temperature was fixed at $T=0.04 \text{ eV}$.

Finally, the complex structure of the order parameter on the hole FS, obtained by solving the linearized Eliashberg equation using the pairing interaction proportional to the RPA spin susceptibility, was approximated by the following function:

$$\Delta_h(\theta, \phi) = 2\bar{\Delta}_h \left\{ \cos(2\theta)^4 + 0.5 \bar{\sin}\left(\phi + \frac{\pi}{3}\right) \Theta\left(-\phi + \frac{2\pi}{3}\right) + \sin\left(\phi + \frac{\pi}{3}\right) \Theta\left(\phi - \frac{2\pi}{3}\right) \right\}$$

where θ and ϕ are the azimuth and the inclination angles in the k space, respectively; $\bar{\Delta}_h$ is the average value of the energy gap on the hole-like FS (equal to $\Delta_h^{\max}/3$), and Θ is the Heaviside step function. The $\Delta_h(\theta, \phi)$ function, together with the constant order parameter on the electron-like FS Δ_e , is plotted in Fig. 3a (gridded surfaces) and used in the 3D BTK fit of the experimental data.

References

- [1] Kamihara, Y. & Watanabe, T. & Hirano, M. & Hosono, H. Iron-Based Layered Superconductor $\text{LaO}_{1-x}\text{F}_x\text{FeAs}$ ($x = 0.05\text{-}0.12$) with $T_c = 26$ K. *J. Am. Chem. Soc.* **130**, 3296 (2008).
- [2] Rotter, M. & Tegel, M. & Johrendt, D., Superconductivity at 38K in the iron arsenide $\text{Ba}_{1-x}\text{K}_x\text{Fe}_2\text{As}_2$, *Phys. Rev. Lett.* **101**, 107006 (2008).
- [3] Lumsden, M. D. & Christianson, A. D., Magnetism in Fe-based superconductors, *J. Phys.: Condens. Matter* **22**, 203203 (2010).
- [4] Mazin, I. I. & Singh, D. J. & Johannes, M. D. & Du, M. H. Unconventional Superconductivity with a Sign Reversal in the Order Parameter of $\text{LaFeAsO}_{1-x}\text{F}_x$. *Phys. Rev. Lett.* **101**, 057003 (2008).
- [5] Liu, D. et al., Electronic origin of high-temperature superconductivity in single-layer FeSe superconductor. *Nat. Commun.* **3**, 931 (2012).
- [6] Tafti, F. F. & Juneau-Fecteau, A. & Delage, M-È. & René de Cotret, S. and Reid, J-Ph. & Wang, A. F. & Luo, X-G. & Chen, X. H. & Doiron-Leyraud, N. & Taillefer, L. Sudden reversal in the pressure dependence of T_c in the iron-based superconductor KFe_2As_2 . *Nature Physics* **9**, 349–352 (2013).
- [7] Qian, T. & Wang, X.-P. & Jin, W.-C. & Zhang, P. & Richard, P. & Xu, G. & Dai, X. & Fang, Z. & Guo, J.-G. & Chen, X.-L. & Ding, H. Absence of a Holelike Fermi Surface for the Iron-Based $\text{K}_{0.8}\text{Fe}_{1.7}\text{Se}_2$ Superconductor Revealed by Angle-Resolved Photoemission Spectroscopy. *Phys. Rev. Lett.* **106**, 187001 (2011).
- [8] Torikachvili, M. S. & Bud'ko, S. L. & Ni, N. & Canfield, P. C. Pressure Induced Superconductivity in CaFe_2As_2 . *Phys. Rev. Lett.* **101**, 057006 (2008).
- [9] Park, T. & Park, E. & Lee, H. & Klimczuk, T. & Bauer, E. D. & Ronning, F. & Thompson, J. D. Pressure-induced superconductivity in CaFe_2As_2 . *J. Phys.: Condens. Matter* **20**, 322204 (2008).
- [10] Dhaka, R. S. & Jiang, Rui & Ran, S. & Bud'ko, S. L. & Canfield, P. C. & Harmon, B. N. & Kaminski, A. & Tomić, M. & Valentí, R. & Lee, Y. Dramatic changes in the electronic structure upon transition to the collapsed tetragonal phase in CaFe_2As_2 . *Phys. Rev. B* **89**, 020511 (R) (2014).
- [11] Gofryk, K. & Saporov, B. & Durakiewicz, T. & Chikina, A. & Danzenbächer, S. & Vyalikh, D. V. & Graf, M. J. & Sefat, A. S. Fermi-Surface Reconstruction and Complex Phase Equilibria in CaFe_2As_2 . Preprint, arXiv:1404.1095 (2014).
- [12] Soh, J. H. & Tucker, G. S. & Pratt, D. K. & Abernathy, D. L. & Stone, M. B. & Ran, S. & Bud'ko, S. L. & Canfield, P. C. & Kreyssig, A. & McQueeney, R. J. & Goldman, A. I. Inelastic Neutron Scattering Study of a Nonmagnetic Collapsed Tetragonal Phase in Nonsuperconducting CaFe_2As_2 : Evidence of the Impact of Spin Fluctuations on Superconductivity in the Iron-Arsenide Compounds. *Phys. Rev. Lett.* **111**, 227002 (2013).
- [13] Pratt, D. K et al. Suppression of antiferromagnetic spin fluctuations in the collapsed phase of CaFe_2As_2 . *Phys. Rev. B* **79**, 060510(R) (2009).
- [14] Yu, W. & Aczel, A. A. & Williams, T. J. & Bud'ko, S. L. & Ni, N. & Canfield, P. C. & Luke, G. M. Absence of superconductivity in single-phase CaFe_2As_2 under hydrostatic pressure. *Phys. Rev. B* **79**, 020511(R) (2009).
- [15] Sanna, A. & Profeta, G. & Massidda, S. & Gross, E. K. U. First-principles study of rare-earth-doped superconducting CaFe_2As_2 . *Phys. Rev. B* **86**, 014507 (2012).
- [16] Prokeš, K. & Kreyssig, A. & Ouladdiaf, B. & Pratt, D. K. & Ni, N. & Bud'ko, S. L. & Canfield, P. C. & McQueeney, R. J. & Argyriou, D. N. & Goldman, A. I. Evidence from neutron diffraction for superconductivity in the stabilized tetragonal phase of CaFe_2As_2 under uniaxial pressure. *Phys. Rev. B* **81**, 180506(R) (2010).
- [17] Saha, S. R. & Butch, N. P. & Drye, T. & Magill, J. & Ziemak, S. & Kirshenbaum, K. & Zavalij, P. Y. & Lynn, J. W. & Paglione, J. Structural collapse and superconductivity in rare-earth-doped CaFe_2As_2 . *Phys. Rev. B* **85**, 024525 (2012).
- [18] Naidyuk, Y. & Yanson, I.K. Point-contact spectroscopy, Springer series in Solid State Sciences, vol. 145. Springer; 2004.
- [19] Daghero, D. & Gonnelli, R.S. Probing multiband superconductivity by point-contact spectroscopy. *Supercond. Sci. Technol.* **23**, 043001 (2010).

- [20] In order to investigate whether such ZBCPs can be due to scattering from impurities, we performed model calculations by solving a three-band $s\pm$ version of the Eliashberg equations, and we found that: a) the impurity level should be extremely high and incompatible with the very high quality of our crystals ; b) even in case of such a large amount of impurities the shape of the ZBCPs would be quite different from the experimental findings.
- [21] Kashiwaya, S. & Tanaka, Y., Tunnelling effects on surface bound states in unconventional superconductors, *Rep. Prog. Phys.* **63**, 1641 (2000).
- [22] Coldea, A. I. & Andrew, C.M.J. & Analytis, J.G. & McDonald, R.D. & Bangura, A.F. & Chu, J.-H. & Fisher, I.R. & Carrington, A., Topological change of the Fermi surface in ternary iron pnictides with reduced c/a ratio: a de Haas-van Alphen study of CaFe_2P_2 , *Phys. Rev. Lett.* **103**, 026404 (2009).
- [23] Daghero, D. & Tortello, M. & Ummerino, G.A. & Gonnelli, R.S. Directional point-contact Andreev-reflection spectroscopy of Fe-based superconductors: Fermi surface topology, gap symmetry, and electron–boson interaction. *Rep. Prog. Phys.* **74**, 124509 (2011).
- [24] Colonna, N. & Profeta, G. & Continenza, A. & Massidda, S., Structural and magnetic properties of CaFe_2As_2 and BaFe_2As_2 from first-principles density functional theory, *Phys. Rev. B* **83** 094529 (2011).
- [25] Suzuki, K. & Usui, H. & Kuroki, K. Possible three dimensional nodes in the $s\pm$ superconducting gap of $\text{BaFe}_2(\text{As}_{1-x}\text{P}_x)_2$. *J. Phys. Soc. Jpn.* **80**, 013710 (2011).
- [26] The calculation of the OP symmetry has been carried out for one specific value of the c/a ratio (1.3826, i.e. at T^*) and thus one pressure (i.e. ~ 0.5 GPa) but qualitatively holds also for the other pressures used in the PCARS experiments, as long as the XZ and YZ hole bands, which provide the largest contribution to the DOS, are filled at Γ while the outer holelike FS survives.
- [27] Matusiak, M. & Bukowski, Z. & Karpinski, J. Nernst effect in single crystals of the pnictide superconductor $\text{CaFe}_{1.92}\text{Co}_{0.08}\text{As}_2$ and parent compound CaFe_2As_2 . *Phys. Rev. B* **81**, 020510(R) (2010).
- [28] Perdew J. P., Burke K. and Ernzerhof M., Generalized Gradient Approximation Made Simple. *Phys. Rev. Lett.* **77** 3865 (1996).
- [29] <http://www.wien2k.at/>
- [30] <http://elk.sourceforge.net/>
- [31] Marzari N. and Vanderbilt D., Maximally localized generalized Wannier functions for composite energy bands. *Phys. Rev. B* **56** 12847 (1997); Souza I., Marzari N. and Vanderbilt D., Maximally localized Wannier functions for entangled energy bands. *Phys. Rev. B* **65** 035109 (2001).
- [32] <http://www.wannier.org>
- [33] <http://www.pwscf.org/>
- [34] Iimura, S. & Matuishi, S. & Sato, H. & Hanna, T. & Muraba, Y. & Kim, S. W. & Kim, J. E. & Takata, M. & Hosono, H., Two-dome structure in electron-doped iron arsenide superconductors. *Nat. Commun.* **3**, 943 (2012).

ACKNOWLEDGMENTS

This work was supported by the Collaborative EU-Japan Project “IRON SEA” (NMP3-SL-2011-283141). R.S.G. wishes to thank the Max-Planck Institute for Solid State Research in Stuttgart where the measurements were carried out.

Corresponding author

Correspondence and requests for materials should be addressed to Renato S. Gonnelli (renato.gonnelli@polito.it).

Author contributions

Z.B. and J. K. grew and characterized the crystals; R.S.G., R.K.K. and P.G.R. designed and set up the experiment; R.S.G. performed the point-contact measurements; G.P. made the ab-initio DFT

calculations; K.S. and K.K. performed the 10 orbital model construction and the RPA analysis; G.A.U., D.D., M.T. and R.S.G. analyzed the experimental results; R.S.G. , D.D. and G.P. wrote the paper.

Competing financial interests

The authors declare that they have no competing financial interests.

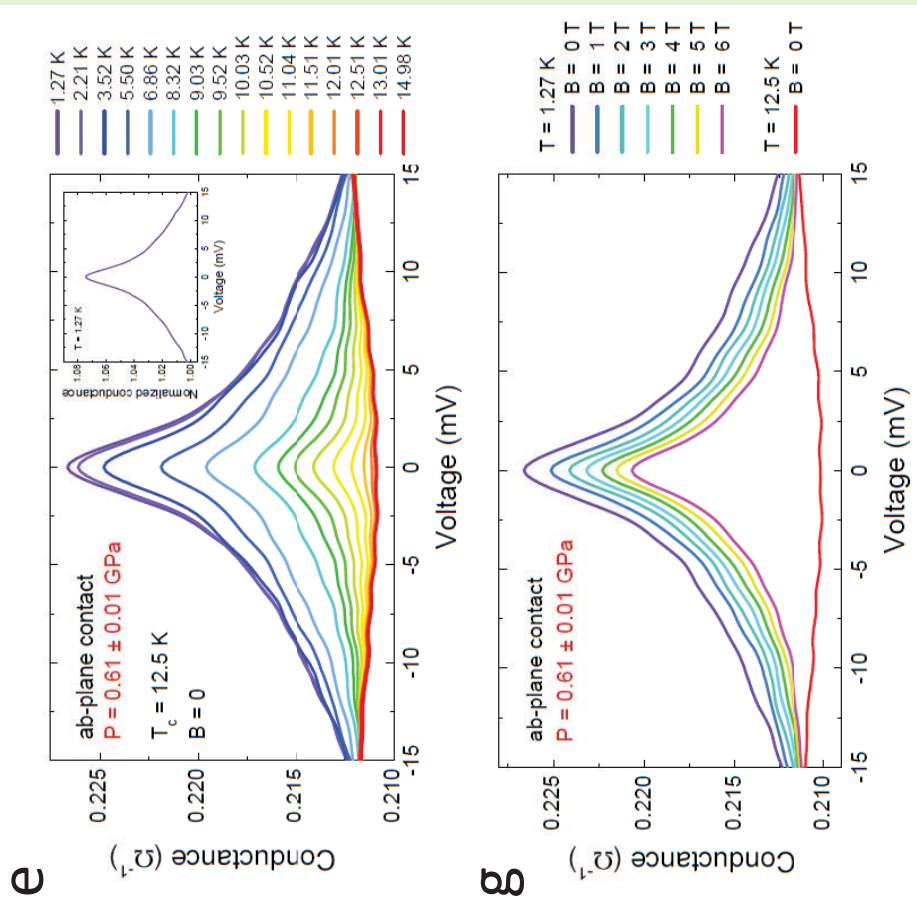
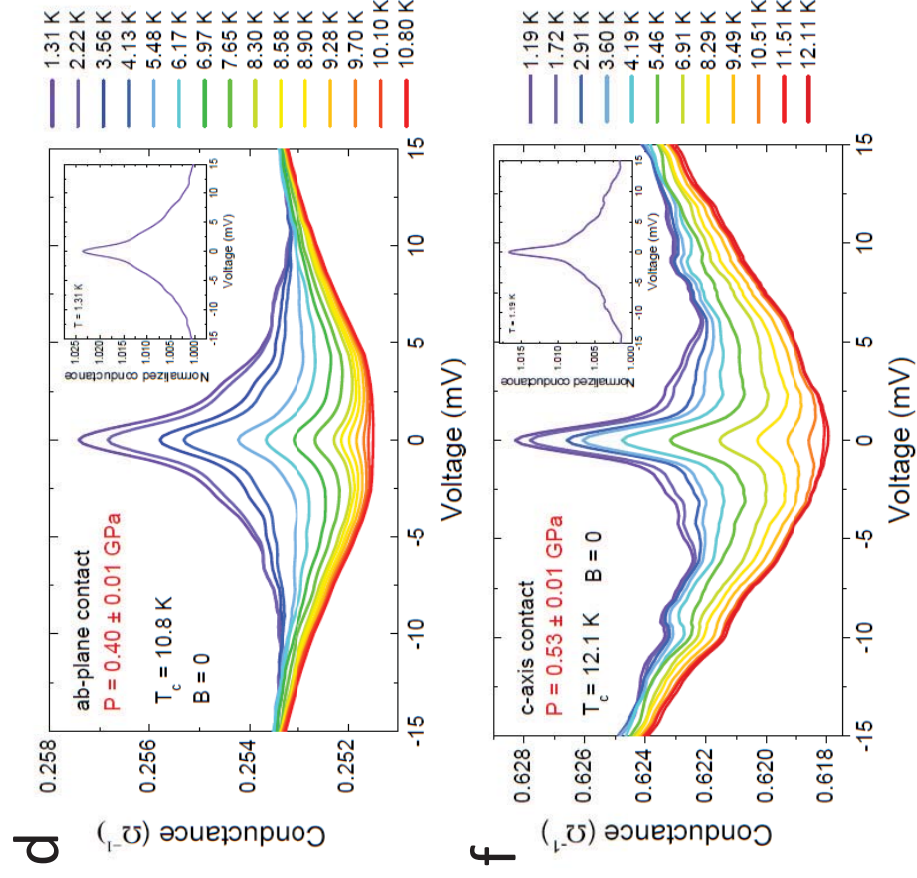
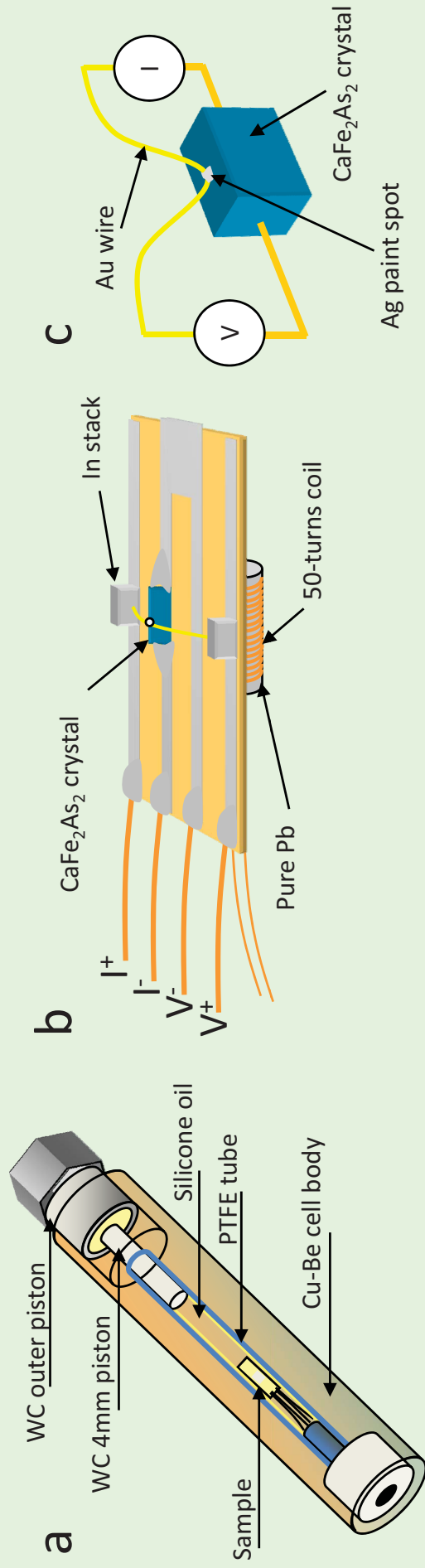
Figure 1 | Scheme of the experimental setup and examples of PCARS spectra. **a**, Drawing of the pressure cell used for the measurements. **b**, Detail of the crystal mounting on a fiberglass board. The crystal is kept in place by In stacks that also provide electrical connection. On the rear of the board is a 50-turns coil wrapped around a piece of high-purity Pb, whose critical temperature (measured by an ac mutual inductance technique) is used to determine the pressure. **c**, Scheme of the crystal with the point contact and of the electric circuit for PCARS measurements: A probe current I is injected into the crystal and the voltage drop V across the contact is measured. **d, e**, Two examples of raw (as-measured) differential conductance curves (dI/dV vs. V) of ab -plane contacts (i.e. contacts in which the probe current is preferentially injected parallel to the ab planes). The curves are measured at various temperatures, in zero magnetic field and at a fixed pressure, i.e. 0.40 ± 0.01 GPa and 0.61 ± 0.01 GPa, respectively. **f**, Temperature dependence of the differential conductance of a c -axis point contact (in which the current is injected mainly along the c axis) in zero magnetic field and at a pressure of 0.53 ± 0.01 GPa. In d, e and f the inset reports the normalized low-temperature conductance, i.e. the PCARS spectrum. **g**, Magnetic-field dependence of the conductance of a ab -plane contact in a pressure of 0.61 ± 0.01 GPa. All the curves were measured at $T=1.27$ K apart from the bottom one, which represents the normal-state conductance measured just above the critical temperature.

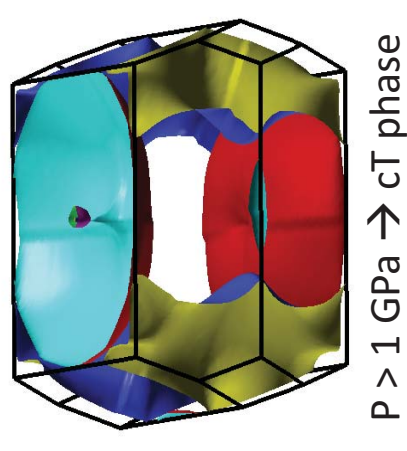
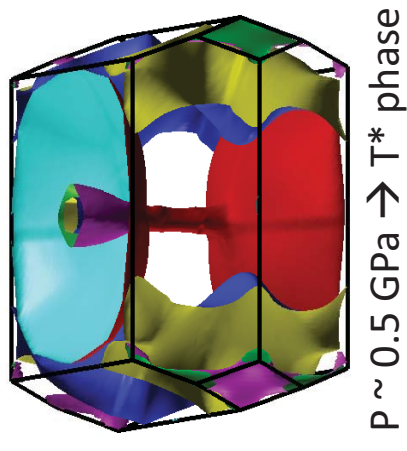
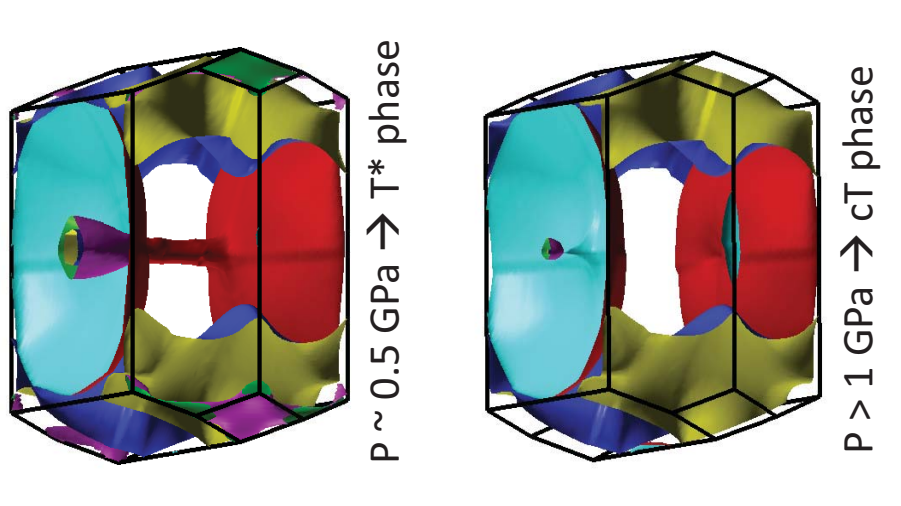
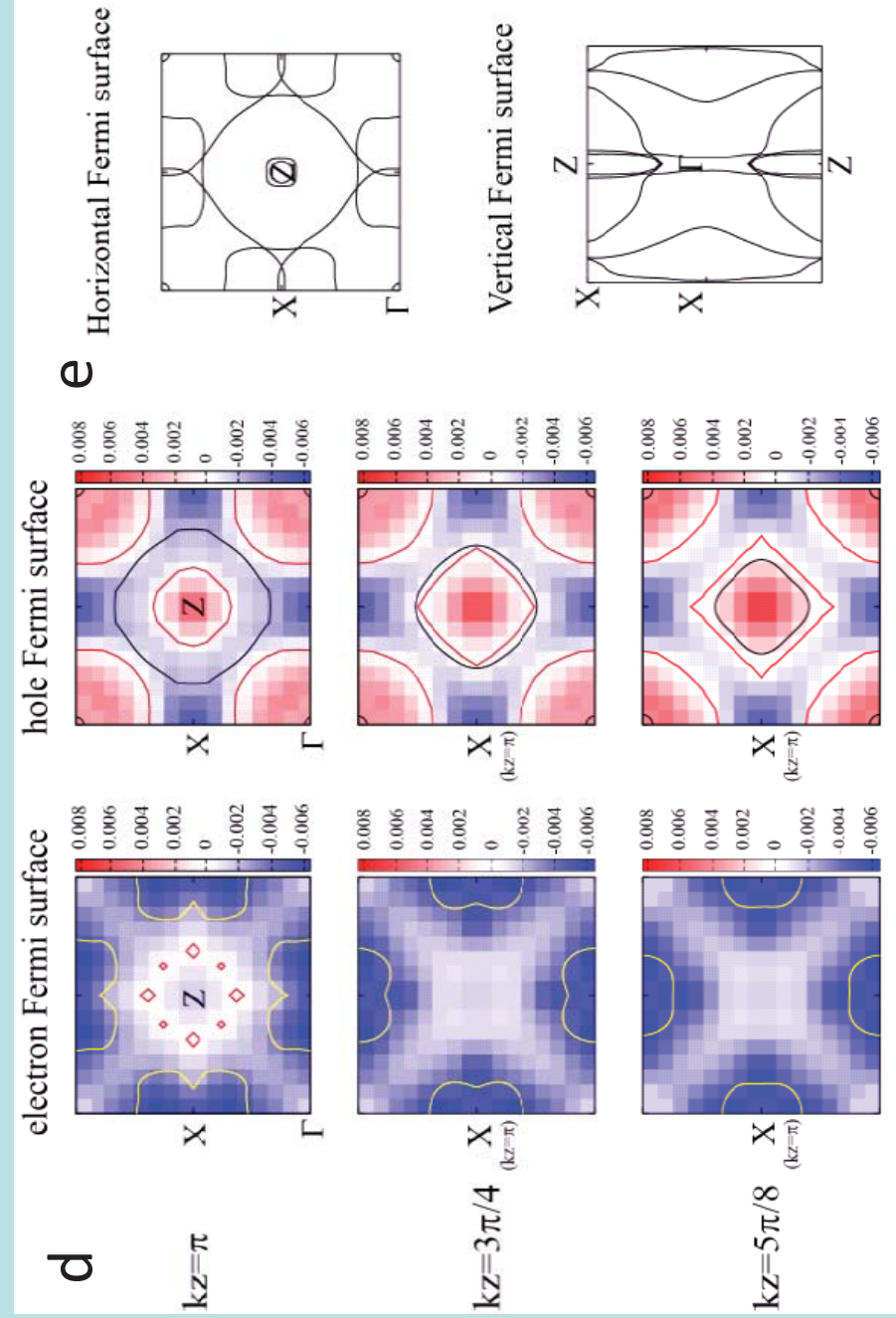
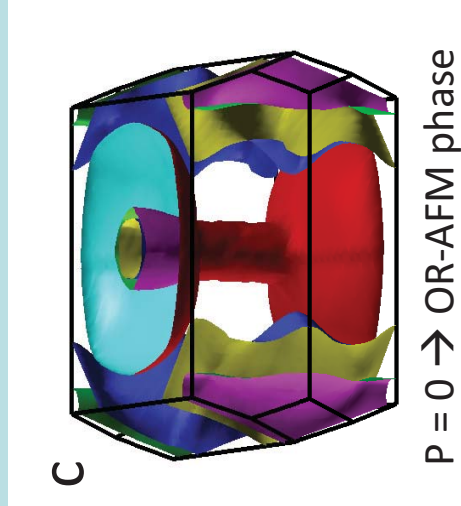
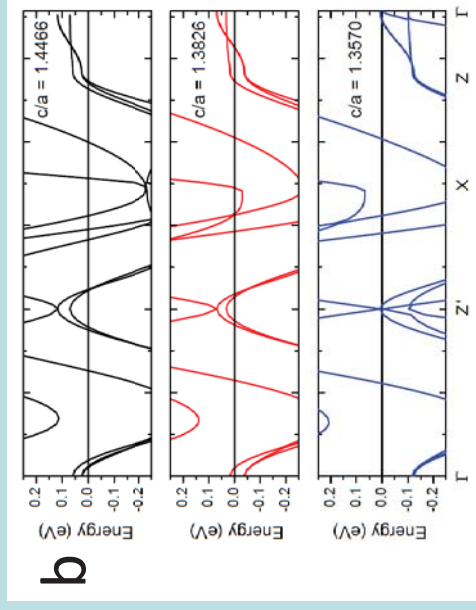
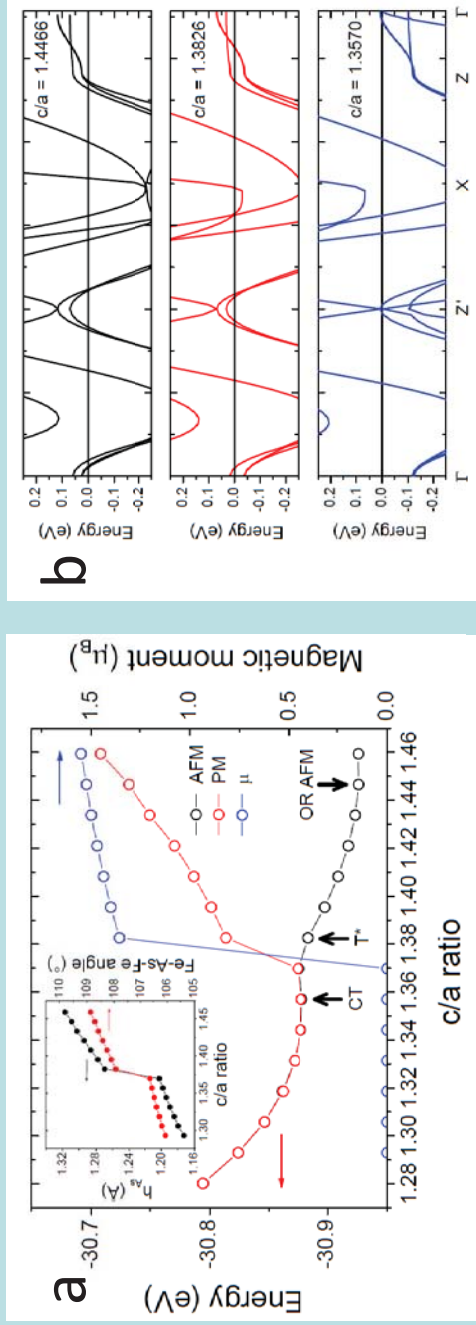
Figure 2 | Electronic bandstructure and calculated order parameters. **a**, Total energy of the crystal calculated by DFT in both the antiferromagnetic (AFM) and paramagnetic (PM) phases as a function of the c/a ratio. The values of c/a that correspond to the orthorhombic (OR), collapsed tetragonal (cT) and low-temperature tetragonal (T^*) phases are indicated by arrows. The magnetic moment is also shown in the main panel while the inset shows the dependence on the c/a ratio of the height of the As ion above the Fe layer (h_{As}) and of the angle made by Fe-As-Fe bonds. **b**, electronic band structure of CaFe_2As_2 in the vicinity of the Fermi level, in the equilibrium structure at ambient pressure (OR AFM, top panel), at the beginning of the pressure-induced phase transition (T^* phase, middle panel) and in the equilibrium cT phase (bottom panel). **c**, The Fermi surface in the three lattice structures, showing that the T^* phase is on the verge of a topological transition of the outer holelike Fermi surface sheet. In the cT phase this sheet is split into two separate pockets. **d**, Calculated superconducting order parameter (OP) at different k_z values for the outer electronlike FS sheets (left) and the outer holelike FS sheet (right), in the T^* phase. The profile of the electronlike (holelike) FS is indicated by white (black) lines; red lines indicate instead

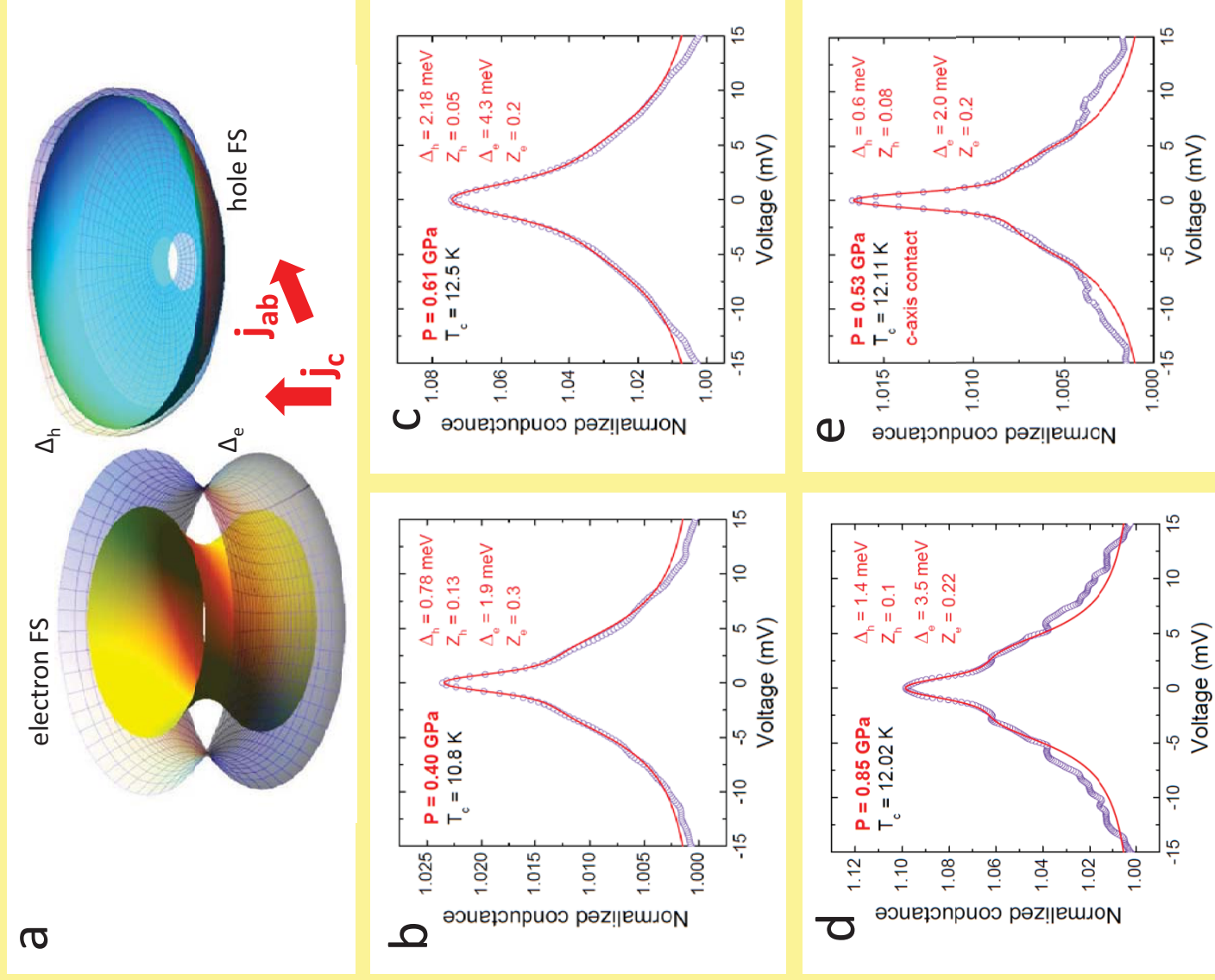
the node lines, i.e. the lines across which the OP changes sign. **e**, Horizontal and vertical cuts of the Fermi surface in the T^* phase.

Figure 3 | Fit of the experimental spectra with the 3D BTK model. **a**, Model FS used in the 3D BTK model (matt surfaces). Here only the upper half of the Brillouin zone is shown. The electronlike FS sheet is schematized by a hyperboloid of revolution while the holelike sheet is represented by a half spheroid (the small cylindrical portion of the FS around the Γ point can be neglected). The gridded surface superimposed to the FS represent the superconducting OP, which is isotropic on the electronlike FS but shows both in-plane anisotropy and a horizontal line of nodes on the holelike FS. **b**, **c**, **d**, Low-temperature PCARS spectra (symbols) of ab -plane contacts at $P= 0.4$ GPa (b), 0.61 GPa (c) and 0.85 GPa (d) with the relevant 3D BTK fit (lines). The fitting parameters are indicated in the legends. **e**, Low-temperature spectrum of a c -axis contact in a pressure of 0.53 GPa, with the relevant fit.

Figure 4 | Pressure dependence of the critical temperature and of the gap amplitudes. **a**, The critical temperature of the contact T_c^A (black squares, right vertical scale) and the gap amplitudes Δ_e and Δ_h (orange and purple circles, left vertical scale), as a function of pressure. **b**, Pressure dependence of the gap ratios $2\Delta_e/k_B T_c$ (orange circles) and $2\Delta_h/k_B T_c$ (purple circles). In both **a** and **b**, data obtained from ab -plane and c -axis contacts are shown as solid and open symbols, respectively. The error bars of the gaps shown in panel **a** are determined by evaluating the maximum possible range of Δ_e and Δ_h values compatible with a given curve, when all the other fitting parameters are changed as well.







R.S. Gonelli et al., Figure 4

